

## Photogrammetric processing of hyperhemispherical images with off-the-shelf solutions

Antonio M. G. Tommaselli<sup>1</sup>, Wimerson Bazan<sup>2,3</sup>, Leticia F. Castanheiro<sup>4</sup>, Mariana B. Campos<sup>5</sup>, Thaisa A.C. Garcia<sup>2</sup>, Maurício Galo<sup>1</sup>

1 Department of Cartography, Faculty of Sciences and Technology, São Paulo State University (UNESP),  
São Paulo 19060-900, Brazil, {a.tommaselli, mauricio.galo}@unesp.br

2 Graduate Program in Cartographic Sciences, Faculty of Sciences and Technology, São Paulo State University (UNESP),  
São Paulo 19060-900, Brazil, {wimerson.bazan, thaisa.correia}@unesp.br

3 Coordination Unit for Geomatics, Federal Institute of Espírito Santo (IFES),  
Espírito Santo 29040-780, Brazil, wimerson.bazan@ifes.edu.br

4 Embrapa Digital Agriculture, Campinas, São Paulo, Brazil - leticia.castanheiro@colaborador.embrapa.br

5 Department of Remote Sensing and Photogrammetry, Finnish Geospatial Research Institute (FGI), National Land Survey of  
Finland (NLS), Espoo, mariana.campos@nls.fi

**KEY WORDS:** Fisheye camera, Hyperhemispherical lenses, Self-calibrating bundle adjustment, Mobile Mapping, HBIM.

### ABSTRACT

The recent availability of off-the-shelf commercial cameras equipped with dual-fisheye lenses, each featuring a hyperhemispherical field of view exceeding 180°, has significantly advanced research addressing a long-standing challenge in Heritage Building Information Modelling (HBIM): the accurate, cost-effective image-based surveying in narrow and spatially constrained environments within Scan-to-BIM workflows. However, advances in digital sensor technology alone do not guarantee the production of accurate HBIM models. Beyond data completeness, HBIM requires high-accuracy modelling with sub-centimetre precision. Achieving such precision through photogrammetric workflows requires rigorous control at every stage of data processing, including camera calibration and 3D reconstruction. However, accuracy analysis can often be overlooked when using highly automated commercial software solutions. To fully exploit the wide field of view of dual-fisheye cameras, in terms of both completeness and final accuracy, an appropriate modelling of hyperhemispherical (HH) lenses using dedicated projection models is essential. This requirement has been a major barrier to the widespread adoption of such cameras in HBIM workflows, given the limited availability of commercial photogrammetric solutions that can properly process dual-fisheye imagery. This paper evaluates the calibration and 3D reconstruction accuracy of a 360° dual-fisheye camera (Ricoh Theta Z1) for surveying a narrow space, using fisheye projection models (equidistant and equisolid-angle) recently implemented in Agisoft Metashape. This represents an important advance in Scan-to-BIM workflows using fisheye imagery, offering a user-friendly, accessible software solution that builds on prior community research that highlighted the importance and benefits of explicitly modelling hyperhemispherical lenses. Thus, this practical study aims to provide insights for the HBIM community by demonstrating how low-cost 360° cameras, when rigorously modelled, can be effectively employed in high-precision Scan-to-HBIM workflows. Results show that the equisolid-angle model achieved higher accuracy, both with 180° FoV images and HH images.

### 1. Introduction

A non-subjective digital record of the historical, physical, and temporal characteristics of cultural monuments and buildings is a fundamental form of preservation, as it captures the state of architectural heritage at a specific moment in time. The creation of such records has long been challenging due to the absence of standardised methods, reliable protocols, and consistent criteria for data quality assessment (Campos et al., 2015). Recent developments in Heritage Building Information Modelling (HBIM) continue to address these limitations by proposing structured documentation approaches that integrate geometric data, historical documentation, and metadata within a single digital environment (Ewart and Zuecco, 2019). A core component of the HBIM workflow is a detailed three-dimensional survey conducted prior to modelling (Murphy et al., 2013). This process, well established within the photogrammetric community, has recently been referred to as Scan-to-BIM, which uses 3D survey techniques to generate point clouds that serve as an accurate geometric database for HBIM model development (Alshawabkeh et al., 2024).

As discussed by Radanovic et al. (2020), digital 3D capture with reliable reproduction of architectural features is the first and most difficult step toward defining an accurate HBIM, particularly in environments and spaces with complex architecture. For instance, narrow staircases, spiral passageways, confined spaces,

interconnected vaults, underground systems, multi-level interiors, and highly decorated environments are especially difficult to document using conventional terrestrial laser scanning and standard perspective imagery (Cui and Wu, 2025). These conditions require extensive acquisition planning, time-consuming surveying, and highly complex data-processing workflows. As a result, the accuracy and completeness of 3D reconstructions are often affected by inappropriate object–sensor distances, frequent occlusions, shadowed areas, and complex spatial configurations. In such contexts, sensors with wider fields of view and improved spatial coverage in constrained environments, such as those using fisheye lenses, have increasingly been adopted as complementary alternatives over the past two decades.

Early technical papers discussed the advantages of using cameras equipped with fisheye lenses, particularly their ability to reduce the required number of images and to provide effective access to constrained or confined spaces. Kedzierski and Waczykowski (2007) discussed the advantages of using fisheye lenses in a narrow alley within the interior courtyard of Warsaw's Town Hall, in Poland. These authors showed that covering the area required 86 perspective images, whereas only 8 fisheye images were sufficient to achieve comparable results. In a subsequent study on the surveying of Warsaw's Old Town, Kedzierski et al. (2009) discussed the effectiveness of fisheye lenses for mapping hard-to-reach cultural heritage objects, highlighting fisheye-

equipped cameras as a valuable documentation tool. During the first decade of the 21st century, research on the use of fisheye lenses in photogrammetry remained limited. At that time, only a few fisheye lens manufacturers had produced acceptable lenses, and a dedicated data acquisition and processing method was still required. Despite the limited number of studies, cameras combined with fisheye lenses have already been recognised as a promising solution for surveying narrow, constrained spaces, particularly compared with traditional photogrammetric surveys. From around 2015 onwards, the availability of commercial cameras equipped with dedicated fisheye lenses significantly boosted studies focused on addressing the long-standing challenge of surveying narrow and constrained spaces using image-based approaches (Covas et al., 2015; Marčič et al., 2016; Perfetti et al., 2017; Alessandri et al., 2019; León-Vega and Rodríguez-Laitón, 2019).

More recently, cameras designed with fisheye lenses have become progressively smaller, more compact, and more stable, while lenses have achieved increasingly wider fields of view, some exceeding 180° Field of View (FoV). Some commercial models integrate dual-fisheye cameras, enabling the capture of full-hemisphere images with adequate resolution and geometric accuracy. Examples of such cameras are Ricoh Theta Z1 (Ricoh Theta Z1, 2026), Insta360 (Insta360, 2025) and GoPro Max360 (GoPro MAX 360, 2025). Most of the omnidirectional cameras mentioned use two fisheye lenses, each with a FoV exceeding 180°, allowing the full sphere to be captured simultaneously through overlap between the two lenses' coverage. Lenses with a field of view wider than 180° are referred to as hyperhemispherical (HH) lenses (Pernechele, 2016).

These developments enabled the easy integration of fisheye cameras into Scan-to-BIM data acquisition plans (Ladai et al., 2022; Herban et al., 2022; Wee et al., 2024; Perfetti et al., 2024; Rezaei and Arefi, 2025), mobile mapping platforms, including backpack systems (Campos et al., 2019; Castanheiro et al., 2020), handheld devices (Perfetti et al., 2024) and UAV's (Yastikli and Özerdem, 2017; Perfetti et al., 2019).

However, advances in digital sensor technology do not automatically guarantee the creation of accurate HBIM models, which often require sub-centimetric precision. As noted by Campos et al. (2015), achieving such precision through photogrammetric workflows requires careful control at every stage of data processing, including camera calibration, a step often overlooked by some authors. Nocerino et al. (2014) highlighted that, despite the growing number of Structure from Motion (SfM) algorithms for 3D reconstruction, many commercial digital reconstruction methods prioritise full automation at the expense of rigorous modelling. This emphasis can reduce the reliability of the resulting models if careful analysis is not conducted, particularly in black-box software environments where quality metrics are unavailable. For instance, to fully exploit the complete field of view of these cameras, accurate modelling of dual-fisheye lenses using a specific projection model is essential (see Section 2). Tommaselli et al. (2023) evaluated points in the hyperhemispherical (HH) field that cause blunders in bundle adjustment (BA), depending on the mathematical model used. Therefore, points in the HH field are often removed either during keypoint detection or by applying a mask that excludes the HH field from the images. The previous assessments were conducted through self-implemented models, highlighting a major limitation to the widespread use of cameras with HH lenses in HBIM workflows: the lack of commercial solutions for the photogrammetric processing of such images.

The majority of recent related work reviewed here relied on commercial software for camera calibration and 3D point cloud generation, such as Metashape and Pix4D. Those photogrammetric software were not originally designed to properly handle images acquired with HH lens geometry and points in the HH image field. Consequently, utilising the full field of view of omnidirectional cameras often leads to reduced accuracy when an inappropriate mathematical model is used, requiring advanced programming skills to implement a rigorous model within a photogrammetric pipeline. For example, some studies performed camera calibration as a separate step, which can, overall, limit the adoption of HH images in routine HBIM workflows.

To address this limitation, and particularly for professional applications, photogrammetric software packages have only recently implemented projection models suitable for HH fisheye lenses. Agisoft Metashape (Agisoft Metashape, 2025) implemented a complete photogrammetric pipeline from the initial relative orientation, in-situ camera calibration, and the generation of dense surface models, and ortho-mosaics, using the equidistant projection model. Subsequently, in version 2.3.0 (Agisoft Metashape, 2026), the equidistant fisheye and equisolid-angle fisheye camera models, with support for hyperhemispheric lenses, were added to the Camera Calibration dialogue. Therefore, we hypothesise that, with this extension, higher-accuracy results can be achieved by exploring the complete HH FoV, as points in the hyperhemispherical field can be correctly modelled and included in the BA rather than discarded.

To investigate this hypothesis, this paper experimentally evaluates the calibration of a 360° dual-fisheye camera (Ricoh Theta Z1) and the 3D reconstruction accuracy of a narrow corridor using the fisheye projection models (equidistant and equisolid) recently implemented in Agisoft Metashape. The Ricoh Theta Z1, which features two HH lenses, may offer significant advantages for scan-to-HBIM in terms of cost, stability, and user-friendly data-acquisition. By evaluating a commercial photogrammetric software pipeline with this camera, the study aims to provide practical insights for the HBIM community, discussing the potential of low-cost 360° cameras, when properly modelled, for use in scan-to-HBIM workflows that require greater accuracy.

## 2. Background

Fisheye lens models are usually designed by projecting points on a sphere onto the image plane using orthogonal, stereographic, equidistant, or equisolid-angle projections (Schneider et al., 2009). Table 1 presents the projection models with their respective mapping functions suitable for fisheye images (Hughes et al., 2010), in which  $f$  is the focal length,  $\alpha$  is the incident angle, and  $r_p$  is the radial distance.

Projection	Mapping function
Orthogonal	$r_p = f \cdot \sin(\alpha)$
Stereographic	$r_p = 2 \cdot f \cdot \tan(\alpha/2)$
Equidistant	$r_p = f \cdot \alpha$
Equisolid-angle	$r_p = 2 \cdot f \cdot \sin(\alpha/2)$

Table 1. Fisheye projection models.

The orthogonal projection is defined as the perpendicular projection of a point on the sphere onto the image plane and is

suitable only for hemispherical fisheye lenses (FoV < 180°), as highlighted by Hughes et al. (2010) and Pernechele (2016).

The stereographic model projects a point to the opposite tangential point of the image plane, which is less common in fisheye lenses. The most used model for fisheye images is equidistant projection (Abraham and Förstner, 2005; Campos et al., 2018; Perfetti et al., 2018; Gao et al., 2020; Gunes et al., 2025).

Due to its widespread use, robustness, and practical relevance, the equidistant model was previously adopted by commercial software, such as Agisoft Metashape, for processing fisheye images. Equation 1 shows the mathematical model based on equidistant projection. A minor modification to the notation is adopted by Agisoft Metashape, as presented in Tommaselli et al. (2023).

$$\begin{aligned} x &= -f \cdot \frac{X_c}{\sqrt{X_c^2 + Y_c^2}} \cdot \text{atan} \left( \frac{\sqrt{X_c^2 + Y_c^2}}{Z_c} \right) \\ y &= -f \cdot \frac{Y_c}{\sqrt{X_c^2 + Y_c^2}} \cdot \text{atan} \left( \frac{\sqrt{X_c^2 + Y_c^2}}{Z_c} \right) \end{aligned} \quad (1)$$

in which:

$X_c, Y_c, Z_c$  are 3D coordinates of a point in the camera reference system;

$f$  is the camera focal length; and

$x, y$  are the coordinates projected to the image plane and correspond to the observed values.

Some studies have shown the limitations of generic models, such as the Extended Unified Camera Model (EUCM) (Garcia et al., 2023; Khomutenko et al., 2016) and some rigorous models, particularly the equidistant projection model, when processing images acquired with HH fisheye lenses (Campos et al., 2018; Perfetti et al., 2018; Castanheiro et al., 2021; Tommaselli et al., 2023; Gunes et al., 2025). To mitigate this problem, points beyond 180° FoV are excluded in some photogrammetric processing steps, such as camera calibration and 3D reconstruction (Perfetti et al., 2018; Campos et al., 2019). Castanheiro et al. (2021) demonstrated the effect of including HH points when using an equidistant model during the calibration of a HH fisheye lens camera with a 190° FoV. The calibration process yielded an RMSE of 17.83 pixels for image residuals when including the HH points, whereas an RMSE of 0.27 pixels was obtained when excluding the HH points. Comparing the four fisheye projection models (orthographic, stereographic, equidistant and equisolid-angle) for the camera calibration of a 190° FoV fisheye lens camera, Castanheiro et al. (2021) concluded that the equisolid-angle model presented the best results. A simultaneous dual-fisheye camera calibration was performed to assess the effect of using HH points to estimate relative orientation parameters in a multi-camera system (Ricoh Theta S). The inclusion of HH points in the camera calibration improved the Relative Orientation Parameters (ROPs) estimation, which was feasible only when using the equisolid-angle projection model.

Later, Tommaselli et al. (2023) also demonstrated a loss of accuracy when using the original HH images in BA with the equidistant model. Their results showed reductions of approximately 50–90% in planimetric accuracy and 40–75% in altimetric accuracy, depending on the calibration strategy and control point configuration. Therefore, the inclusion of HH points requires either excluding points when using the equidistant projection model or employing an alternative projection model, such as the equisolid-angle model, as suggested by Castanheiro et al. (2021).

Garcia et al. (2023) implemented the equisolid-angle projection model in ORB-SLAM and compared its performance with the

EUCM (Khomutenko et al., 2016) for HH images, concluding that the equisolid-angle model presented better results.

The previous findings showing the limitations of the equidistant model motivated the implementation of the equisolid-angle model in the last release of Agisoft Metashape (Agisoft Metashape, 2026). Equation 2 presents the mathematical model for equisolid-angle projection.

$$\begin{aligned} x &= 2f \cdot \frac{X_c}{\sqrt{2(X_c^2 + Y_c^2)}} \cdot \sqrt{1 - \frac{Z_c}{X_c^2 + Y_c^2 + Z_c^2}} \\ y &= 2f \cdot \frac{Y_c}{\sqrt{2(X_c^2 + Y_c^2)}} \cdot \sqrt{1 - \frac{Z_c}{X_c^2 + Y_c^2 + Z_c^2}} \end{aligned} \quad (2)$$

Due to lens distortions, image coordinates ( $x, y$ ) are usually computed using a fisheye projection model combined with distortion models, such as the Conrady-Brown model (Brown, 1971). In Agisoft Metashape, distortions are modelled using Conrady-Brown's distortion model, combined with the affinity and shear parameters (Fraser, 1997), as presented in Equation 3 (Agisoft Metashape, 2026).

$$\begin{aligned} \Delta x &= x(K_1 r^2 + K_2 r^4 + K_3 r^6 + K_4 r^8) + P_1(r^2 + 2x^2) + 2P_2 xy + B_1 x + B_2 y \\ \Delta y &= y(K_1 r^2 + K_2 r^4 + K_3 r^6 + K_4 r^8) + P_2(r^2 + 2y^2) + 2P_1 xy \end{aligned} \quad (3)$$

in which:

$x$  and  $y$  are the image coordinates;

( $K_1, K_2, K_3, K_4$ ) are the coefficients of the radial symmetric distortions;

( $P_1, P_2$ ) are the decentering distortion coefficients; and

( $B_1, B_2$ ) are the affinity and shear distortions coefficients.

### 3. Dataset and experiments

#### 3.1 Data acquisition

This imaging system consists of two back-to-back fisheye lenses (Figure 1.a), each with a 196° FoV (hyperhemispherical geometry), a focal length of 2.5 mm, and two 1" CMOS sensors, resulting in a pixel size of 2.41  $\mu\text{m}$  (Ricoh Theta Z1, 2026). The original raw still images have a dimension of 7296 x 3648 pixels and are cropped into two frames of 3648 x 3648 pixels (Figure 1.b and 1.c), corresponding to each camera for later photogrammetric processing.

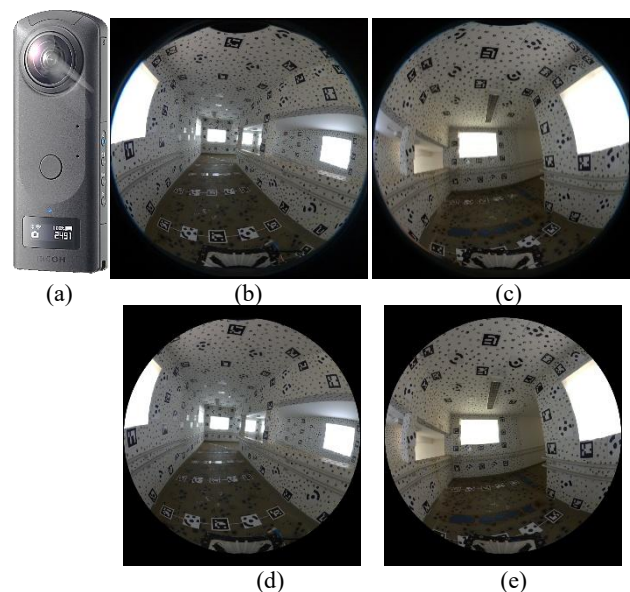


Figure 1. (a) Ricoh Theta Z dual-fisheye camera; (b) and (c) full images from sensors 1 and 2; (d) and (e) corresponding images cropped to a 180° FoV.

Dual-fisheye frames were acquired with the Ricoh Theta Z1 dual-fisheye camera in still mode in a 360° calibration field composed of ArUco (in yellow) and circular coded targets (in red), as depicted in Figure 2.a. In addition, 6 control and 14 check distances were measured between some of these points for use in the processing step (Figure 2.b). These distances were measured with a PANTEC 2000 mm / 80" calliper.

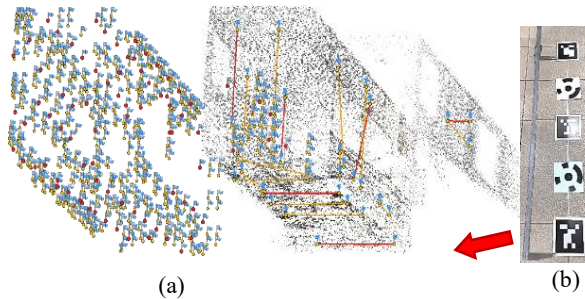


Figure 2. (a) Calibration Field (ArUco in blue and circular target in red); (b) Measured distances used as control (lines in red) and check (lines in yellow).

### 3.2 Data processing and experiments' design

A total of 31 dual-fisheye still frames were collected at different positions and orientations to cover the area from multiple viewpoints and to reduce correlations among exterior and interior orientation parameters. After cropping the original still frames into two separate images with HH FoV (Figure 1.a and Figure 1.b), yielding 62 images, both cameras were calibrated using Agisoft Metashape (Agisoft Metashape, 2026) under different configurations (Table 1). Distances among some target corners were measured with a precision calliper and used as control and check entities, as depicted in Figure 2.b (6 distances as control and 14 as check entities).

To evaluate both 180° and 196° fields of view (HH) images, two datasets were used in this study: (1) 62 images acquired from Sensor 1 (S1; 31 images) and Sensor 2 (S2; 31 images); and (2) cropped images derived from the same 62 original images, with the HH field removed, thus, having the same exterior orientation. Those datasets were used in the Experiments 1 to 6 as summarised in Table 1.

Exps. #	Exp. 1	Exp. 2	Exp. 3	Exp. 4	Exp. 5	Exp. 6
Var.						
FoV	180°			196°		
Camera model	Equid.	Equis.	Equid.	Equis.	Equid.	Equis.
Use of sensors (s1/s2)	Simultaneous processing				Independent processing	
Images per processing	62			31 (two procs.)		
Tie-points	72,340		79,100		33,895 (s1)/ 30,240 (s2)	
Control distances	6					
Check distances	14					

Table 1. Experiments' configurations and variables considered.

Considering the images with a 180° FoV, 72,300 tie points were extracted, and camera calibration was performed with the two projection models: first with the equisolid-angle model, recently implemented in Agisoft Metashape, with automatic point filtering applied using a threshold of 0.02 m on the estimated

standard deviation from the covariance matrix. Subsequently, the same set of tie points and project configurations was used to run the camera calibration process for the equidistant model (Experiments 1 and 2).

The original images with the wider FoV (196°) were then processed in Agisoft Metashape, resulting in 79,100 tie-points (same filtering strategy with a threshold of 0.02 m on the estimated standard deviation from the covariance matrix) with the same setup and camera models (Experiments 3 and 4).

In the Experiments 1 to 4, the self-calibrating bundle adjustment was performed with two sensors simultaneously, in which the same Exterior Orientation Parameters (EOPs) are estimated for each image pair, but with two different sets of Interior Orientation Parameters (IOPs) for each sensor. A further set of experiments (Exp. 5 and 6) was conducted, considering each set of images from each sensor as separate image blocks for the BA. With this sensor-independent configuration, it was possible to extract 33,895 and 30,240 tie points for sensors 1 and 2, respectively. These image blocks were used to calibrate the sensors in two independent processing with FoV = 196° for both camera models (Experiments 5 and 6).

Experiments with different numbers of distortion coefficients were also conducted, and it was observed that including  $K_4$  in the radial lens distortion model improved results, most likely due to severe distortions at image boundaries. Thus, this set of 4 coefficients was used in all experiments. Similar experiments were performed, including the  $B_1$  and  $B_2$  affine coefficients. It was concluded that these two parameters were not significant in the case studied and were therefore not considered in the remaining experiments. The discussion of the contribution and significance of each coefficient in the final results and the improvements is beyond the scope of this work and is left for future research.

### 4. Results and discussion

The results are summarised in Tables 2, 3 and 4 and Figures 3 and 4. Figure 3 and Tables 2 and 3 evidence the reduction of the estimated standard deviation of the IOPs when using the equisolid-angle model (Exp. 2) for 180° FoV. On the other hand, the equisolid-angle model performs much better (Exp. 4) than the equidistant (Exp. 3) when the images with the full HH field are considered, i.e., with FoV = 196°.

Exp. #	Exp. 1	Exp. 2	Exp. 3	Exp. 4	Exp. 5	Exp. 6
IOP						
$f$ (px)	1082.13	1076.64	1088.33	1078.95	1086.81	1078.22
$\sigma$	$\pm 0.036$	$\pm 0.034$	$\pm 0.039$	$\pm 0.032$	$\pm 0.048$	$\pm 0.038$
$c_x$ (px)	5.5238	5.5962	5.8584	5.8644	5.7532	5.9018
$\sigma$	$\pm 0.035$	$\pm 0.03$	$\pm 0.041$	$\pm 0.028$	$\pm 0.057$	$\pm 0.038$
$c_y$ (px)	4.0648	3.6037	3.6835	3.2259	6.6326	6.2547
$\sigma$	$\pm 0.045$	$\pm 0.037$	$\pm 0.053$	$\pm 0.035$	$\pm 0.085$	$\pm 0.055$
$K_1$ (px <sup>-2</sup> )	0.2593	0.3476	0.2221	0.3306	0.2257	0.3316
$\sigma$	$\pm 0.00015$	$\pm 0.00018$	$\pm 0.00014$	$\pm 0.00015$	$\pm 0.00017$	$\pm 0.00017$
$K_2$ (px <sup>-4</sup> )	-0.3006	-0.3819	-0.2358	-0.3462	-0.2394	-0.3467
$\sigma$	$\pm 0.00024$	$\pm 0.00033$	$\pm 0.00018$	$\pm 0.00023$	$\pm 0.00022$	$\pm 0.00027$
$K_3$ (px <sup>-6</sup> )	0.1360	0.1984	0.0942	0.1705	0.0956	0.1704
$\sigma$	$\pm 0.00014$	$\pm 0.00024$	$\pm 9.3e-05$	$\pm 0.00015$	$\pm 0.00011$	$\pm 0.00017$
$K_4$ (px <sup>-8</sup> )	-0.0229	-0.0393	-0.0140	-0.0320	-0.0142	-0.0319
$\sigma$	$\pm 3e-05$	$\pm 5.9e-05$	$\pm 1.6e-05$	$\pm 3.2e-05$	$\pm 2e-05$	$\pm 3.8e-05$
$P_1$ (px <sup>-1</sup> )	3.5e-05	3.5e-05	5.2e-05	5.8e-05	5.8e-05	4.4e-05
$\sigma$	$\pm 2.9e-06$	$\pm 2.8e-06$	$\pm 3.3e-06$	$\pm 2.7e-06$	$\pm 4.6e-06$	$\pm 3.7e-06$
$P_2$ (px <sup>-1</sup> )	-0.0019	-0.0023	0.0019	-0.00221	-0.0022	-0.0025
$\sigma$	$\pm 4.1e-06$	$\pm 3.9e-06$	$\pm 4.8e-06$	$\pm 3.8e-06$	$\pm 7.5e-06$	$\pm 5.8e-06$

Table 2. Estimated IOPs and standard deviation for sensor 1 (s1), considering six experiments.

<i>Exp. #</i> <i>IOP</i>	<i>Exp. 1</i> ( <i>s2</i> )	<i>Exp. 2</i> ( <i>s2</i> )	<i>Exp. 3</i> ( <i>s2</i> )	<i>Exp. 4</i> ( <i>s2</i> )	<i>Exp. 5</i> ( <i>s2</i> )	<i>Exp. 6</i> ( <i>s2</i> )
$f$ (px)	1080.32	1074.74	1086.42	1076.86	1086.29	1077.18
$\sigma$	$\pm 0.038$	$\pm 0.037$	$\pm 0.042$	$\pm 0.034$	$\pm 0.053$	$\pm 0.042$
$c_x$ (px)	3.8078	4.3741	3.8625	4.3706	2.9197	3.4795
$\sigma$	$\pm 0.035$	$\pm 0.029$	$\pm 0.040$	$\pm 0.027$	$\pm 0.056$	$\pm 0.038$
$c_y$ (px)	4.5191	4.1643	4.1626	3.7634	2.2988	1.8862
$\sigma$	$\pm 0.045$	$\pm 0.037$	$\pm 0.054$	$\pm 0.036$	$\pm 0.091$	$\pm 0.060$
$K_1(px^{-2})$	0.2627	0.3520	0.2266	0.3364	0.2278	0.3357
$\sigma$	$\pm 0.00016$	$\pm 0.00019$	$\pm 0.00015$	$\pm 0.00015$	$\pm 0.00019$	$\pm 0.00019$
$K_2(px^{-4})$	-0.3026	-0.3853	-0.2406	-0.3530	-0.2420	-0.3520
$\sigma$	$\pm 0.00025$	$\pm 0.00034$	$\pm 0.00016$	$\pm 0.00024$	$\pm 0.00024$	$\pm 0.0003$
$K_3(px^{-6})$	0.1364	0.1995	0.0966	0.1743	0.0971	0.1735
$\sigma$	$\pm 0.00015$	$\pm 0.00025$	$\pm 9.7e-05$	$\pm 0.00015$	$\pm 0.00012$	$\pm 0.00019$
$K_4(px^{-8})$	-0.0229	-0.0393	-0.0145	-0.0328	-0.0145	-0.0325
$\sigma$	$\pm 3e-05$	$\pm 6.1e-05$	$\pm 1.7e-05$	$\pm 3.3e-05$	$\pm 2.1e-05$	$\pm 4.2e-05$
$P_1(px^{-1})$	0.0012	0.0014	0.0012	0.0014	0.0013	0.0015
$\sigma$	$\pm 2.9e-06$	$\pm 2.8e-06$	$\pm 3.3e-06$	$\pm 2.7e-06$	$\pm 4.8e-06$	$\pm 3.9e-06$
$P_2(px^{-1})$	-0.0008	-0.0009	-0.0008	-0.0009	-0.0007	-0.0007
$\sigma$	$\pm 4.2e-06$	$\pm 4.0e-06$	$\pm 4.9e-06$	$\pm 3.9e-06$	$\pm 8.0e-06$	$\pm 6.4e-06$

Table 3. Estimated IOPs and standard deviation for sensor 2 (*s2*), considering six experiments.

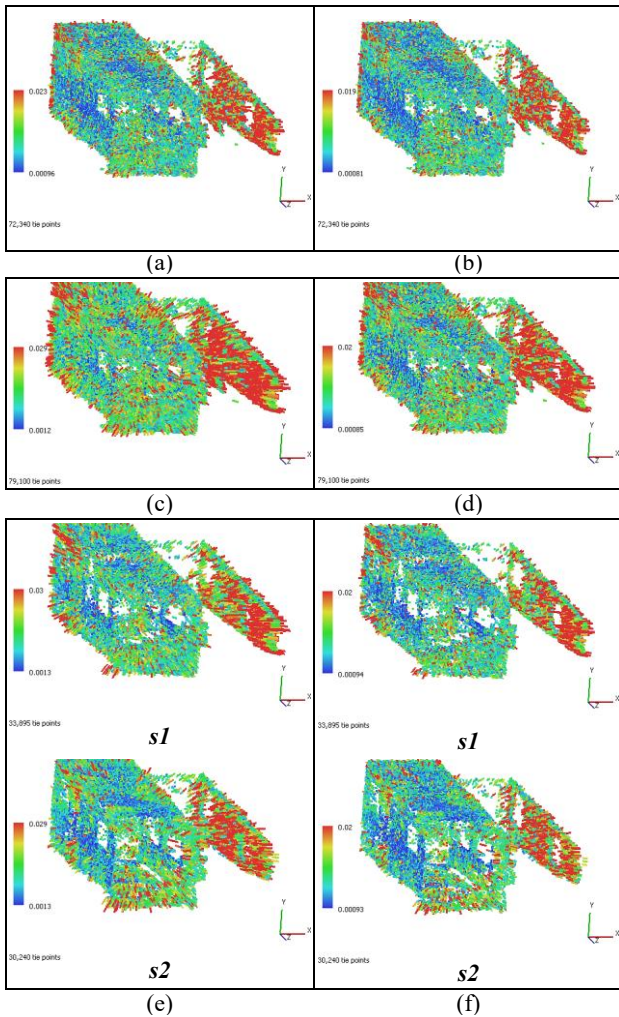


Figure 3. (a) Estimated standard deviations of tie-points coordinates across experiments: (a) Exp. 1, (b) Exp. 2, (c) Exp. 3, (d) Exp. 4, (e) Exp. 5 and (f) Exp. 6 .

From the analysis of Tables 2 and 3, it can be seen that the estimated value of the parameters also changes depending on the projection model used. The values of the camera focal length estimated with the equidistant and equisolid models differ by

approximately 8 pixels; the values estimated with HH images are slightly different from those estimated with 180° FoV images for the same projections model. Some variations were also observed in the principal point coordinates, particularly for the  $c_y$  component, in the experiment with separate runs.

In Figure 3 the estimated standard deviations of the tie-points are graphically represented. These vectors indicate the direction and value of the largest semi-axis of the error ellipsoid given by the estimated covariance matrix in BA (Agisoft Metashape, 2026). It can be observed that the magnitudes of these estimated errors are larger in experiments in which the equidistant model was used (Figures 3.a, 3.c and 3.e) in comparison to the equisolid-angle model (Figures 3.a, 3.c and 3.e).

For the images cropped with 180° FoV, the differences were negligible, but for the HH images, it is notable the improvements when using the equisolid-angle model. Figure 4 presents the residuals in the image coordinates for the same group of experiments, for sensors 1 and 2. It can be seen that the magnitude of the residuals follows a similar pattern, as observed for the estimated standard deviations of the 3D coordinates of the tie points. Again, the best results were achieved with the equisolid-angle model, both for the 180° FoV images and for the HH images.

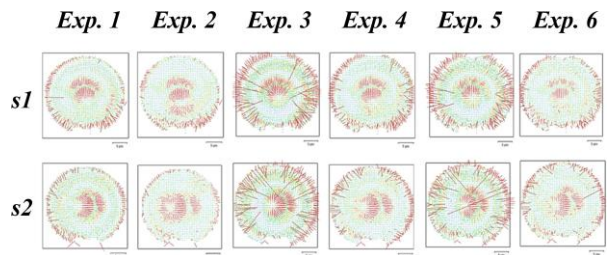


Figure 4. Graphical residuals for sensor 1 (*s1*) and 2 (*s2*) across six experiments.

Table 4 presents some quantitative metrics for the six experiments. The total errors in control and check distances were also lower when using the equisolid model (Table 4). The total reprojection errors, the RMSE of residuals for both sensors 1 and 2 and the total errors in control and check points are always large for the experiments with the equidistant model.

<i>Exp. #</i> <i>Metrics</i>	<i>Exp. 1</i>	<i>Exp. 2</i>	<i>Exp. 3</i>	<i>Exp. 4</i>	<i>Exp. 5</i>		<i>Exp. 6</i>	
					<i>s1</i>	<i>s2</i>	<i>s1</i>	<i>s2</i>
<b>Total reproj. error (px)</b> <i>max</i>	1.07	0.94	1.37	1.01	1.29	0.94	13.51	11.51
	12.39	12.89	8.76	12.78	1.30	0.95	23.30	10.18
<b>RMSE of resids. for sensor 1 (px)</b> <i>max</i>	0.61	0.41	1.24	0.628	0.96	0.52	9.04	3.76
	6.68	3.09	13.80	4.90				
<b>RMSE of resids. for sensor 2 (px)</b> <i>max</i>	0.56	0.38	1.30	0.65	1.17	0.58	23.30	8.12
	4.48	2.75	13.9	5.21				
<b>Total error in control dist. (mm)</b> <i>max abs.</i>	0.49	0.49	0.82	0.39	1.70	0.92	2.98	1.92
	0.67	0.76	1.71	0.59	2.08	0.72	3.76	1.24
<b>Total error in check dist. (mm)</b> <i>max abs.</i>	2.75	2.53	2.91	2.53	2.76	2.53	6.30	6.74
	6.91	6.67	6.63	6.49	3.52	2.61	6.35	5.47

Table 4. Metrics estimated after the calibration procedure for six experiments.

## 5. Conclusions

This paper presents an experimental assessment of the equidistant and equisolid-angle models, implemented in Agisoft Metashape, for the photogrammetric processing of images collected with fisheye cameras. In particular, the suitability of these models as implemented in Agisoft Metashape for images generated by hyperhemispherical cameras was assessed. The accuracy achieved in the experiments presented in this paper is fully compatible with the requirements for scan-to-HBIM, which typically range between  $\pm 5$  mm and  $\pm 20$  mm (Banfi, 2019; Brusaporci et al., 2023).

The main conclusion was that the equisolid-angle projection model implemented in Agisoft Metashape can correctly handle hyperhemispherical images, enabling camera calibration and further 3D modelling with higher accuracy than with the equidistant model.

The omnidirectional cameras, such as the Ricoh Theta Z1, assessed in this work, have significant potential thanks to the current processing software in many applications. Further research can be conducted on open topics, such as the optimal set of IOPs and the calibration of dual-fisheye cameras with relative orientation constraints. The geometry of the network with fisheye images requires further study of the weighting strategies for observations based on intersection angles to avoid problems with points near the infinite and aligned with the sensor trajectory. The results presented in this paper also motivate future assessment of dual fish-eye cameras for scan-to-HBIM using similar methodologies.

## Acknowledgments

This study was funded in part by the São Paulo Research Foundation, FAPESP (2021/06029-7), Coordenação de Aperfeiçoamento de Pessoal de Nível Superior – CAPES (Grant: 88887.961788/2024-00), Conselho Nacional de Desenvolvimento Científico e Tecnológico - CNPq (Grant: 303670\_2018-5), by the Finnish Government (Postdoctoral Programme for Research Institutes in Finland - Tulanet) and Research Council of Finland (Grants: 356137, 359203 and 359204).

## References

Abraham, S., Förstner, W., 2005. Fish-eye-stereo calibration and epipolar rectification. *ISPRS Journal of Photogrammetry and Remote Sensing* 59, 278–288.

Agisoft Metashape, 2026. Agisoft Metashape User Manual - Professional Edition, Version 2.3 [www Document]. URL [https://www.agisoft.com/pdf/metashape-pro\\_2\\_3\\_en.pdf](https://www.agisoft.com/pdf/metashape-pro_2_3_en.pdf)

Agisoft Metashape, 2025. Agisoft Metashape Change Log.

Alessandri, L., Baiocchi, V., Del Pizzo, S., Rolfo, M.F., Troisi, S., 2019. Photogrammetric survey with fisheye lens for the characterization of the La Sassa Cave. *Int. Arch. Photogramm. Remote Sens. Spatial Inf. Sci.* XLII-2/W9, 25–32. <https://doi.org/10.5194/isprs-archives-XLII-2-W9-25-2019>

Alshawabkeh, Y., Baik, A., Miky, Y., 2024. HBIM for Conservation of Built Heritage. *IJGI* 13, 231. <https://doi.org/10.3390/ijgi13070231>

Banfi, F., 2019. The integration of a scan-to-HBIM process in BIM application: the development of an add-in to guide users in Autodesk Revit. *Int. Arch. Photogramm. Remote Sens. Spatial*

*Inf. Sci.* XLII-2/W11, 141–148. <https://doi.org/10.5194/isprs-archives-XLII-2-W11-141-2019>

Brown, D.C., 1971. Close-Range Camera Calibration. *Photogrammetric Engineering* 37, 855–866.

Brusaporci, S., Maiezza, P., Marra, A., Tata, A., Vespasiano, L., 2023. Scan-to-HBIM Reliability. *Drones* 7, 426. <https://doi.org/10.3390/drones7070426>

Campos, M., Tommaselli, A., Ivánová, I., Billen, R., 2015. Data Product Specification Proposal for Architectural Heritage Documentation with Photogrammetric Techniques: A Case Study in Brazil. *Remote Sensing* 7, 13337–13363. <https://doi.org/10.3390/rs71013337>

Campos, M.B., Tommaselli, A.M.G., Castanheiro, L.F., Oliveira, R.A., Honkavaara, E., 2019. A Fisheye Image Matching Method Boosted by Recursive Search Space for Close Range Photogrammetry. *Remote Sensing* 11, 1404. <https://doi.org/10.3390/rs11121404>

Campos, M.B., Tommaselli, A.M.G., Honkavaara, E., Prol, F. dos S., Kaartinen, H., El Issaoui, A., Hakala, T., 2018. A Backpack-Mounted Omnidirectional Camera with Off-the-Shelf Navigation Sensors for Mobile Terrestrial Mapping: Development and Forest Application. *Sensors* 18. <https://doi.org/10.3390/s18030827>

Castanheiro, L.F., Tommaselli, A.M.G., Berveglieri, A., Campos, M.B., Junior, J.M., 2021. Modeling Hyperhemispherical Points and Calibrating a Dual-Fish-Eye System for Close-Range Applications. *Photogrammetric Engineering & Remote Sensing* 87, 375–384. <https://doi.org/10.14358/PERS.87.5.375>

Castanheiro, L.F., Tommaselli, A.M.G., Campos, M.B., Berveglieri, A., Santos, G., 2020. 3D Reconstruction of Citrus Trees Using an Omnidirectional Optical System, in: *2020 IEEE Latin American GRSS ISPRS Remote Sensing Conference (LAGIRS)*. pp. 409–414. <https://doi.org/10.1109/LAGIRS48042.2020.9165687>

Covas, J., Ferreira, V., Mateus, L., 2015. 3D reconstruction with fisheye images strategies to survey complex heritage buildings, in: *2015 Digital Heritage*. IEEE, Granada, pp. 123–126. <https://doi.org/10.1109/DigitalHeritage.2015.7413850>

Cui, H., Wu, J., 2025. How Architectural Heritage Is Moving to Smart: A Systematic Review of HBIM. *Buildings* 15, 2664. <https://doi.org/10.3390/buildings15152664>

Ewart, I.J., Zuecco, V., 2019. Heritage Building Information Modelling (HBIM): A Review of Published Case Studies, in: Mutis, I., Hartmann, T. (Eds.), *Advances in Informatics and Computing in Civil and Construction Engineering*. Springer International Publishing, Cham, pp. 35–41. [https://doi.org/10.1007/978-3-030-00220-6\\_5](https://doi.org/10.1007/978-3-030-00220-6_5)

Fraser, C.S., 1997. Digital camera self-calibration. *ISPRS Journal of Photogrammetry and Remote Sensing* 52, 149–159.

Gao, W., Wang, K., Ding, W., Gao, F., Qin, T., Shen, S., 2020. Autonomous aerial robot using dual-fisheye cameras. *J. Field Robotics* 37, 497–514. <https://doi.org/10.1002/rob.21946>

Garcia, T.A.C., Tommaselli, A.M.G., Castanheiro, L.F., Campos, M.B., 2023. Comparison of two mathematical models for fisheye cameras applied in the ORB-SLAM. *Int. Arch. Photogramm. Remote Sens. Spatial Inf. Sci.* XLVIII-1/W1-2023, 155–160. <https://doi.org/10.5194/isprs-archives-XLVIII-1-W1-2023-155-2023>

- GoPro MAX 360, 2025. GoPro MAX 360 Action Camera (Waterproof + Stabilization) [WWW Document]. URL <https://gopro.com/en/us/shop/cameras/learn/max/CHDZH-203-master.html> (accessed 10.26.25).
- Gunes, U., Turkulainen, M., Kannala, J., Rahtu, E., 2025. Evaluating Fisheye-Compatible 3D Gaussian Splatting Methods on Real Images Beyond 180 Degree Field of View. *ARXIV* <https://doi.org/10.48550/ARXIV.2508.06968>
- Herban, S., Costantino, D., Alfio, V.S., Pepe, M., 2022. Use of Low-Cost Spherical Cameras for the Digitisation of Cultural Heritage Structures into 3D Point Clouds. *J. Imaging* 8, 13. <https://doi.org/10.3390/jimaging8010013>
- Hughes, C., Denny, P., Jones, E., Glavin, M., 2010. Accuracy of fish-eye lens models. *Appl. Opt.* 49, 3338–3347. <https://doi.org/10.1364/AO.49.003338>
- Insta360, 2025. Insta360 Ace Pro 2 – The 8K AI-Powered Action Cam [www Document]. URL <https://www.insta360.com/product/insta360-ace-pro2> (accessed 10.26.25).
- Kedzierski, M., Waczykowski, P., 2007. Fisheye lens camera system application to cultural heritage data acquisition, in: *Proceedings of the 21st CIPA Symposium*. p. 5.
- Kedzierski, M., Walczykowski, P., Fryskowska-Skibniewska, A., 2009. Application of fisheye lens and terrestrial laser scanning in architectonic documentation of hard-to-reach cultural heritage objects. *Proceedings of the ASPRS 2009 Annual Conference*.
- Khomutenko, B., Garcia, G., Martinet, P., 2016. An Enhanced Unified Camera Model. *IEEE Robot. Autom. Lett.* 1, 137–144. <https://doi.org/10.1109/LRA.2015.2502921>
- Ladai, A., Toth, C., Toth, Z., 2022. Indoor mapping with an omnidirectional camera system: performance analysis. *Int. Arch. Photogramm. Remote Sens. Spatial Inf. Sci.* XLIII-B1-2022, 347–352. <https://doi.org/10.5194/isprs-archives-XLIII-B1-2022-347-2022>
- León-Vega, H.A., Rodríguez-Laitón, M.I., 2019. Fisheye lens image capture analysis for indoor 3d reconstruction and evaluation. *Int. Arch. Photogramm. Remote Sens. Spatial Inf. Sci.* XLII-2/W17, 179–186. <https://doi.org/10.5194/isprs-archives-XLII-2-W17-179-2019>
- Marčič, M., Barták, P., Valaška, D., Fraštia, M., Trhan, O., 2016. Use of image based modelling for documentation of intricately shaped objects. *Int. Arch. Photogramm. Remote Sens. Spatial Inf. Sci.* XLI-B5, 327–334. <https://doi.org/10.5194/isprs-archives-XLI-B5-327-2016>
- Murphy, M., McGovern, E., Pavia, S., 2013. Historic Building Information Modelling – Adding intelligence to laser and image based surveys of European classical architecture. *ISPRS Journal of Photogrammetry and Remote Sensing* 76, 89–102. <https://doi.org/10.1016/j.isprsjprs.2012.11.006>
- Nocerino, E., Menna, F., Remondino, F., 2014. Accuracy of typical photogrammetric networks in cultural heritage 3D modeling projects. *Int. Arch. Photogramm. Remote Sens. Spatial Inf. Sci.* XL–5, 465–472. <https://doi.org/10.5194/isprsrarchives-XL-5-465-2014>
- Perfetti, L., Fassi, F., Rossi, C., 2019. Fisheye photogrammetry to generate low-cost DTMs. *Int. Arch. Photogramm. Remote Sens. Spatial Inf. Sci.* XLII-2/W17, 257–263. <https://doi.org/10.5194/isprs-archives-XLII-2-W17-257-2019>
- Perfetti, L., Fassi, F., Vassena, G., 2024. Ant3D—A Fisheye Multi-Camera System to Survey Narrow Spaces. *Sensors* 24, 4177. <https://doi.org/10.3390/s24134177>
- Perfetti, L., Polari, C., Fassi, F., 2017. Fisheye photogrammetry: tests and methodologies for the survey of narrow spaces. *Int. Arch. Photogramm. Remote Sens. Spatial Inf. Sci.* XLII-2-W3, 573–580. <https://doi.org/10.5194/isprs-archives-XLII-2-W3-573-2017>
- Perfetti, L., Polari, C., Fassi, F., Troisi, S., Baiocchi, V., Del Pizzo, S., Giannone, F., Barazzetti, L., Previtali, M., Roncoroni, F., 2018. *Fisheye Photogrammetry to Survey Narrow Spaces in Architecture and a Hypogea Environment*. <https://doi.org/10.3390/books978-3-03842-685-1-1>
- Pernechele, C., 2016. Hyper hemispheric lens. *Opt. Express* 24, 5014. <https://doi.org/10.1364/OE.24.005014>
- Radanovic, M., Khoshelham, K., Fraser, C., 2020. Geometric accuracy and semantic richness in heritage BIM: A review. *Digital Applications in Archaeology and Cultural Heritage* 19, e00166. <https://doi.org/10.1016/j.daach.2020.e00166>
- Rezaei, S., Arefi, H., 2025. Evaluation of Network Design and Solutions of Fisheye Camera Calibration for 3D Reconstruction. *Sensors* 25, 1789. <https://doi.org/10.3390/s25061789>
- Ricoh Theta Z1, 2026. RICOH THETA Z1 [www Document]. URL <https://thetaz1.com/en/> (accessed 1.2.26).
- Schneider, D., Schwalbe, E., Maas, H.-G., 2009. Validation of geometric models for fisheye lenses. *ISPRS Journal of Photogrammetry and Remote Sensing* 64, 259–266.
- Tommaselli, A.M.G., Garcia, T.A.C., Castanheiro, L.F., Campos, M.B., Santos, G.H., 2023. Effects of hyper hemispherical field in Bundle Adjustment with fisheye images. *Int. Arch. Photogramm. Remote Sens. Spatial Inf. Sci.* XLVIII-1/W1-2023, 503–509. <https://doi.org/10.5194/isprs-archives-XLVIII-1-W1-2023-503-2023>
- Wee, T., Tang, K., Farid, M., 2024. Assessment of Low-Cost Digital Camera with Fisheye Lens in Close-Range Photogrammetry for Indoor Building Dimensional Measurement, *Journal of Emerging Technologies and Industrial Applications* 3(1), 1–7.
- Yastikli, N., Özerdem, Ö.Z., 2017. Architectural heritage documentation by using low cost UAV with fisheye lens: Otag-I Humayun in Istanbul as a case study. *ISPRS Ann. Photogramm. Remote Sens. Spatial Inf. Sci.* IV-4/W4, 415–418. <https://doi.org/10.5194/isprs-annals-IV-4-W4-415-2017>